https://doi.org/10.5194/egusphere-2024-3972
Preprint. Discussion started: 20 March 2025

Active-passive microwave scattering in the Antarctica wind-glazed region: an analog for icy moons of Saturn

Léa Elise Bonnefoy[1,2], Catherine Prigent[1,7], Ghislain Picard[3], Clément Soriot[4,1], Alice Le Gall[5,6], Lise Kilic[7,1], and Carlos Jimenez[7,1]

[1]LERMA, Observatoire de Paris, PSL Research University, CNRS, Sorbonne Universités, Univ. Paris Cité, F-75014 Paris, France
[2]LMD/IPSL, Sorbonne Universités, ENS, PSL Research University, Ecole Polytechnique, Institut Polytechnique de Paris, Paris, France
[3]Institut des Géosciences de l'Environnement, Univ. Grenoble Alpes, CNRS, 38000 Grenoble, France
[4]University of Manitoba: Winnipeg, Manitoba, CA
[5]Laboratoire Atmosphères, Milieux, Observations Spatiales (LATMOS), UVSQ/CNRS/Paris VI, UMR 8190, 78280 Guyancourt, France
[6]Institut Universitaire de France, Paris, France
[7]Estellus, 93 boulevard de Sebastopol, 75002 Paris, France

Correspondence: Léa E. Bonnefoy (lb543@cornell.edu)

Abstract. Microwave radiometry and scatterometry, two complimentary modes of sensing the composition and structure of the top meters to hundreds of meters of the subsurface, are often difficult to reconcile, both on the Earth cryosphere and on icy moons of Saturn. To help interpret and model microwave scattering in porous, high-purity ices, we examine jointly 6.9 to 89 GHz AMSR2 radiometry in vertical (V) and horizontal (H) polarizations as well as 5.2 GHz ASCAT, 13.4 GHz QuikSCAT, and 13.5 GHz OSCAT scatterometry in the wind-glazed region of the East Antarctic ice sheet. The data are simulated using the Snow Microwave Radiative Transfer (SMRT) with a simplified snowpack with constant temperature and continuously increasing grain size and density with depth. For the first time, we show that scatterometry and 6.9 to 37 GHz radiometry at V polarization can be successfully simulated with a unique simple snowpack model, indicating that incoherent volume scattering on subsurface heterogeneities dominates both the active and passive signals. To also simulate H-polarized radiometry, a thin surface ice layer as observed in the wind-glazed regions is necessary. Additional complexity, such as seasonal temperature variations, surface roughness, or non-continuous density variations, is necessary to explain the 89 GHz data and HH-polarized backscatter. Meanwhile, applying the same approach to simulate simultaneously passive and active Ku-band observations of icy moons improves on previous attempts but remains unable to reproduce the very high backscatter observed, highlighting the importance of coherent scattering and possibly unknown large (at least millimetric) icy structures in the subsurface.

1 Introduction

Planetary ices on Jupiter and Saturn's icy moons present an anomalous behavior to microwave radars. Indeed, their radar properties include very high backscatter – with Enceladus being the most radar-bright object in the solar system – diffuse scattering, and very high linear and circular polarization ratios (Hapke, 1990; Ostro & Shoemaker, 1990; Ostro et al., 2006, 2010;

https://doi.org/10.5194/egusphere-2024-3972
Preprint. Discussion started: 20 March 2025

Black, 2001; Le Gall et al., 2019; Hofgartner & Hand, 2023). These properties are attributed to volume scattering in a low-loss medium, which is likely enhanced by coherent backscattering (Hofgartner & Hand, 2023, and references therein). However, Janssen et al. (2011); Bonnefoy et al. (2020); Le Gall et al. (2023) highlight another anomalous aspect of microwave scattering on Saturn's icy moons: simple radiative transfer models are unable to simultaneously explain active (radar) and passive (radiometry) observations at the same frequency. Indeed, the Cassini Radar instrument, which operated in the Ku-band (13.78 GHz frequency, 2.2 cm wavelength) measured high backscatter but also higher than expected microwave emissivities (Le Gall et al., 2023).

The surfaces of Saturn's icy moons are constituted primarily of high-purity water ice, with a small quantity of unidentified non-icy material that varies regionally and from moon to moon (e.g., Le Gall et al., 2023, and references therein). Most observations indicate a composition of crystalline water ice, even if at the low surface temperatures (about 60 to 100 K) amorphous water ice would also be stable. At these temperatures, ice is unlikely to melt or metamorphize, although large impacts, micrometeorite gardening, and cryovolcanism can introduce heat and create large, though local and temporary, thermal gradients (Porter et al., 2010). Thermal infrared and microwave radiometry observations point to low thermal inertia and likely loose, porous ice created by impacts reworking the surface into a regolith (Howett et al., 2010; Ries & Janssen, 2015; Howett et al., 2016; Ferrari & Lucas, 2016; Bonnefoy et al., 2020). The very high radar backscatter from both Jupiter's and Saturn's moons is consistent with an icy, porous medium with multiple embedded scattering structures (Le Gall et al., 2019; Hofgartner & Hand, 2023). The high-porosity crystalline water ice of the surface and near-subsurface material (down to unknown depths varying from meters to hundreds of meters) is thus analogous to snow, even though its origin is very different: the impacts of any material onto icy moons (icy E ring dust, Phoebe ring dust, other impactors) occur at very high speeds, thus sand-blasting rather than "snowing on" the surface.

To find an analog of these environments on Earth, we therefore turn to cold, radar-bright snow and porous ice. Until now, Earth analogs used to interpret microwave radar observations of Jupiter's and Saturn's icy moons have included the Greenland percolation zone (Rignot et al., 1993; Rignot, 1995), penitentes in Chile (Hobley et al., 2018), and Northwest Greenland (Culberg et al., 2022). However, all of these analogs present seasonal melt, a process which does not affect icy moons. Herein, we propose a new analog to understand microwave scattering on icy moon surfaces: the Antarctic wind-glazed and megadune regions. More specifically, we focus on the large megadune field southward of Concordia station in the East Antarctic ice sheet (shown in Fig. 1), between 100 and 150°E, which is the least emissive and most scattering region of Antarctica at 19 and 37 GHz (Fahnestock et al., 2000; Picard et al., 2009; Brucker et al., 2010). This region is the coldest and driest area on Earth (Traversa et al., 2023), with average temperatures around -50°C, and is swept by a constant katabatic wind which transports and sublimates snow downslope (Scambos et al., 2012). The snow megadunes are low-amplitude (2–4 m tall), long-wavelength (2–5 km spacing) eolian features with regions of snow accumulation separated by wide wind-glazed zones of near-zero net snow accumulation or even erosion (Frezzotti et al., 2002; Traversa et al., 2023). The glazed areas consist in a millimeter-thick ice crust covering a heavily metamorphized snow with large crystals (Albert et al., 2004; Courville et al., 2007). Due to the low accumulation rates, the snow within the top tens of centimeters to meters is exposed to seasonal temperature variations for decades or centuries, giving time for large hoar crystals to develop despite the low temperatures (Albert et al., 2004; Courville

https://doi.org/10.5194/egusphere-2024-3972
Preprint. Discussion started: 20 March 2025

et al., 2007; Scambos et al., 2012). These large crystals, very scattering at microwave frequencies, are responsible for the observed low emissivities and high radar backscatter (Fahnestock et al., 2000).

The wind-glazed regions of Antarctica have been associated with both high radar backscatter and low microwave emissivities, which are most likely due to large grain sizes in the subsurface (Fahnestock et al., 2000; Brucker et al., 2010). The large, polygonal grains and chains formed by the sublimation-deposition cycles cause important scattering in the subsurface. Because the deeper snow is older, it had time to form larger depth hoar, forming a vertical gradient in grain size (Picard et al., 2022b; Brucker et al., 2010). The depth probed by a microwave radiometer is closely proportional to the wavelength, thus longer wavelengths (i.e., shorter frequencies) probe deeper. However, these longer wavelengths are also sensitive to larger grain sizes, which occur at depth. These two effects compensate each other, and lead to a flat spectrum at 19 to 37 GHz; this effect was successfully modeled by Brucker et al. (2010) using the dense-medium radiative transfer model multi layer model (DMRT-ML) (Picard et al., 2013). Radiative transfer modeling has since been improved with the possibility to simulate active radar data simultaneously, leading to the Snow Microwave Radiative Transfer model (SMRT) thermal emission and radar backscatter model (Picard et al., 2018). This model has recently been applied to a multi-frequency dataset in several regions in Antarctica and the Canadian Arctic, where it is able to successfully reproduce brightness temperatures from 10 to 89 GHz using the subsurface structure measured on site (Picard et al., 2022b). Soriot et al. (2022) used the same model to simulate multi-frequency radiometry and C-band scatterometry over sea ice, highlighting the importance of depth hoar in multi-year sea ice. Herein, we apply this model to the Antarctic wind-glazed regions for the first time to simulate both microwave thermal emission at five frequencies from 6 to 89 GHz and radar backscatter at 5.2 and 13.4 GHz.

The goals of this study are twofold : 1) to use a unique snowpack and radiative transfer model to simulate jointly horizontally (H) and vertically (V) polarized microwave radiometry from 6.9 to 89 GHz and scatterometry at 5.2 and 13.4 GHz in the Antarctica wind-glazed region and 2) to infer novel interpretations on the comparative microwave scattering properties of cold icy surfaces, in Antarctica and on icy moons. In Section 2, we present the datasets used herein, which include observations from AMSR2 (Advanced Microwave Scanning Radiometer), ASCAT (Advanced Scatterometer), OSCAT (Oceansat Scatterometer), and QuikSCAT (Quick Scatterometer). Section 3 details the configuration of the SMRT model used to simulate these data, the snowpack properties, and the model parameters. Section 4 presents the success of the model in reproducing most observations, and the relative importance of each parameter in controlling the different frequencies, polarizations, or observation modes. Finally, Section 5 discusses the validity of the Antarctic megadunes region as an icy moon analog and applies the same method with a two-layer snowpack to attempt to reproduce simultaneously unresolved radar and radiometry observations of Saturn's satellites.

2 Remote sensing data

Most of the radar and microwave radiometry data on Saturn's icy moons were acquired with the Cassini Radar; it was thus crucial for the Earth analog dataset to include both active and passive data in the Ku-band. Other frequencies, both in active and passive, help further constrain the interpretations, properly understand the frequency dependence of parameters like grain size

https://doi.org/10.5194/egusphere-2024-3972
Preprint. Discussion started: 20 March 2025

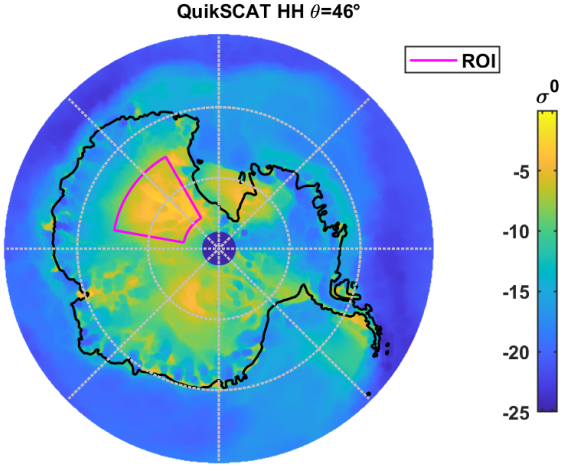

Figure 1. Yearly averaged QuikSCAT 46° incidence HH-polarization view of Antarctica. The region of interest (ROI), which is plotted in magenta, is the most radar-bright region of Antarctica.

and density, and test the capacity of the model to successfully model multi-frequency active and passive data. Frequencies above about 100 GHz probe very shallow depths (Picard et al., 2012) and are not sensitive to the subsurface properties. Meanwhile, over very thick ice and snow, frequencies lower than 2 GHz (available for example with SMOS and SMAP) may require a coherent radiative transfer model to account for interference between layers (Leduc-Leballeur et al., 2015; Tan et al., 2015), whereas the SMRT models only incoherent scattering. We therefore restrict the analyzed data to frequencies from 5.2 to 89 GHz. The AMSR2, ASCAT, OSCAT and QuikSCAT datasets were all averaged over a year and gridded to a uniform resolution of 12.5 km/pixel using the EASE-grid 2.0 Southern hemisphere grid projection (Brodzik et al., 2012, 2014).

To identify dominant behaviors in the active and passive microwave datasets, we use the Kohonen classification algorithm (Kohonen, 1990), previously applied to a similar dataset in the Arctic by Soriot et al. (2022). This unsupervised machine learning algorithm identifies statistically significant clusters, which are self-organized with neighborhood requirements. The classification in 10 clusters is shown in Figs. 2 and 3, whose comparison highlights the anticorrelation between active and passive data, with very radar-bright regions exhibiting low emissivities.

2.1 Multi-frequency radiometry: AMSR2

The passive radiometry data used herein was acquired by the Advanced Microwave Scanning Radiometer (AMSR2) aboard the Japanese polar orbiting satellite GCOM-W. This instrument, which has been operational since 2012, measures the brightness temperature T_B in V and H polarizations at frequencies from 6.9 to 89 GHz at an incidence angle of 55°. The resolution varies from 4 km at 89 GHz to 48 km at 6.9 GHz. Herein, we use the T_B at frequencies of 6.9, 10.65, 18.7, 36.5, and 89 GHz (Maeda et al., 2016), which correspond to wavelengths of 4.4, 2.8, 1.6, 0.82, and 0.34 cm respectively.

https://doi.org/10.5194/egusphere-2024-3972
Preprint. Discussion started: 20 March 2025

Instrument	ASCAT	AMSR2	AMSR2	QuikSCAT	OSCAT	AMSR2	AMSR2	AMSR2
Mode	Acitve	Passive	Passive	Active	Active	Passive	Passive	Passive
Frequency (GHz)	5.2	6.9	10.65	13.4	13.5	18.7	36.5	89.0
Wavelength (cm)	5.8	4.4	2.8	2.2	2.2	1.6	0.82	0.34
Incidence angle	25–65°	55°	55°	46°(HH)	49°(HH)	55°	55°	55°
				54.1°(VV)	57°(VV)			
Polarization	VV	V&H	V&H	VV&HH	VV&HH	V&H	V&H	V&H

Table 1. Instrument frequencies, wavelengths, and incidence angles.

AMSR2 emissivities have been computed using the AMSR2 brightness temperatures L1R data provided by the JAXA at their original spatial resolution for each frequency. The atmospheric contribution has been corrected using the radiative transfer model of Rosenkranz (2017). The inputs used to calculate the atmospheric contribution (air temperature and humidity) have been provided by the ECMWF Reanalysis data (ERA5). The surface temperature needed to compute the emissivity is the skin temperature provided by ERA5 data. To remove seasonal temperature variations, AMSR2 data are averaged over the whole year of 2019. We averaged only emissivities calculated with low cloud liquid water content (less that $0.05\ \mathrm{kg.m^{-2}}$, as indicated by the ERA5 reanalyses) to minimize cloud impact on the observed brightness temperatures. Pixels contaminated by Radio Frequency Interferences (RFI) are also filtered out using the flags provided by the JAXA. This dataset is shown in Fig. 2.

2.2 C-band scatterometry: ASCAT

The Advanced Scatterometer ASCAT aboard the EUMETSAT's MetOp (Meteorological Operational)-A, B, and C satellites operates in VV polarization at 5.2 GHz (C-band), at incidence angles from 25° to 65° and 50 km resolution (Figa-Saldaña et al., 2002). We used the publicly available level-1 calibrated σ^0 measured by ASCAT. Radar observations are not directly sensitive to temperature and change very little with seasons in the region of interest (mean standard deviation=0.04 dB for ASCAT and 0.1 dB for OSCAT and QuikSCAT), but for consistency the ASCAT data were averaged over the year 2019 like the AMSR2 dataset. The ASCAT data are shown in Fig. 3.

2.3 Ku-band scatterometry: QuikSCAT and OSCAT

The SeaWinds instrument aboard QuikSCAT measured the normalized backscatter cross-section σ^0 at 13.4 GHz (Ku-band) in HH polarization at an incidence angle of 46° and VV at 54°, at a resolution of 6×25 km, from 1999 to 2009. The Indian Space Research Organization's Oceansat Scatterometer (OSCAT) instrument aboard OceanSat-2 then ScatSat-1 also operates in Ku-band, at 13.515 GHz. σ^0 is measured in HH polarization at 49° and VV at 57°, at a resolution of 6×30 km. QuikSCAT and OSCAT data are both publicly available on the NASA Scatterometer Climate Record Pathfinder website (www.scp.byu.edu).

We use both datasets to improve coverage in terms of incidence angles; QuikSCAT data is averaged over 2008 and OSCAT over 2018. Although QuikSCAT did not observe over the same years as AMSR2, ASCAT, and OSCAT, the snow cover in

https://doi.org/10.5194/egusphere-2024-3972
Preprint. Discussion started: 20 March 2025

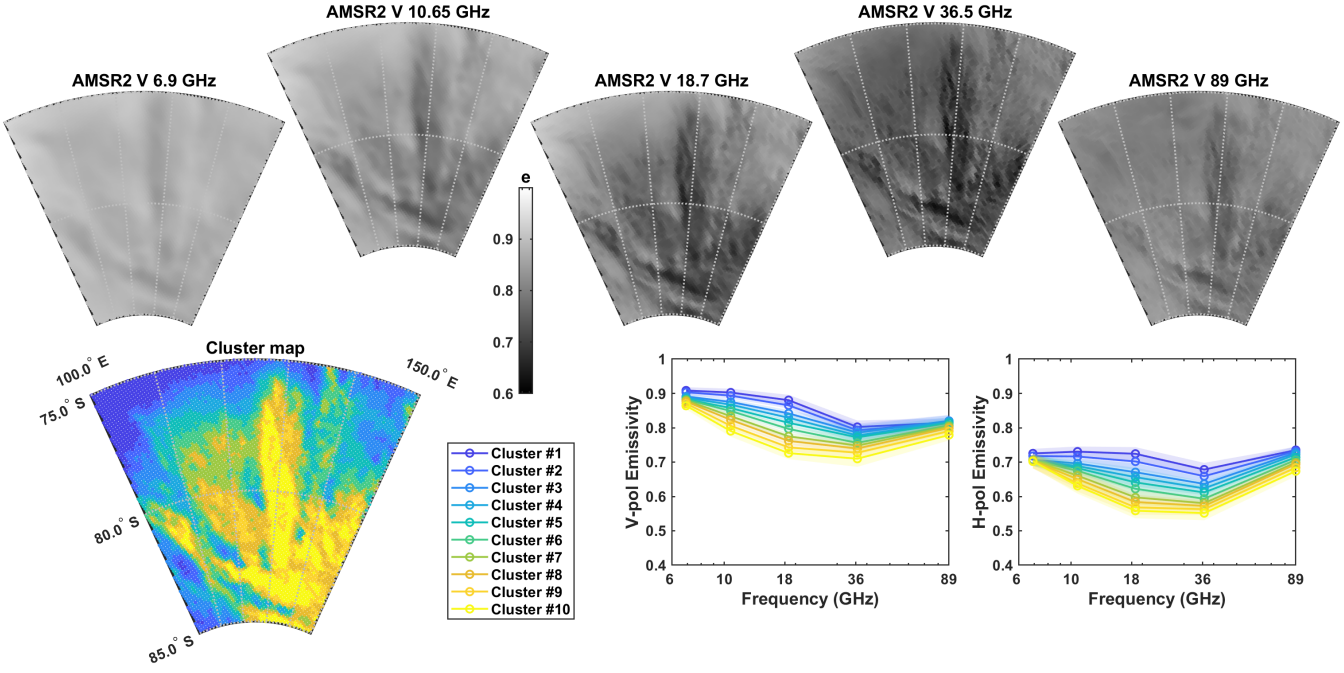

Figure 2. Top: AMSR2 data at 6.9, 10.65, 18.7, 36.5, and 89 GHz in V polarization averaged over the year 2019 in the region of interest. Note the color scale is the same for all frequencies. Bottom: Result of the Kohonen clustering algorithm with 10 clusters. Note that the regions with lowest emissivity (cluster #10, in yellow) correspond to the radar-brightest regions and to the presence of megadunes.

the wind-glazed regions is unlikely to have substantially changed between 2008 and 2019; this is confirmed by the strong consistency between OSCAT and QuikSCAT (Lindell & Long, 2016; Hill & Long, 2017). The QuikSCAT and OSCAT data are shown in Fig. 3. At Ku-band, the radars are more sensitive to embedded scattering structures in the snow (depth hoar) and in the ice (bubbles) than at C-band, explaining the higher backscatter observed in QuikSCAT and OSCAT data than in ASCAT data.

3 Method

3.1 SMRT model configuration

We simulate the scatterometry and radiometry data using the SMRT model (Picard et al., 2018), which is capable of simulating both active and passive microwave data. The snowpack is modeled as a stack of a plane-parallel horizontally infinite layers, each with fixed properties. The SMRT model allows for flexibility in the scattering model, the radiative transfer solver, and the microstructure model applied to each layer. Our specific choices and configuration are described below.

We use the symmetrized scaled strong contrast expansion theory (SymSCE) recently proposed by Picard et al. (2022a) based on theoretical work by Torquato & Kim (2021). This choice is explained by the fact that at 10 to 30 meter depths, which are

https://doi.org/10.5194/egusphere-2024-3972
Preprint. Discussion started: 20 March 2025

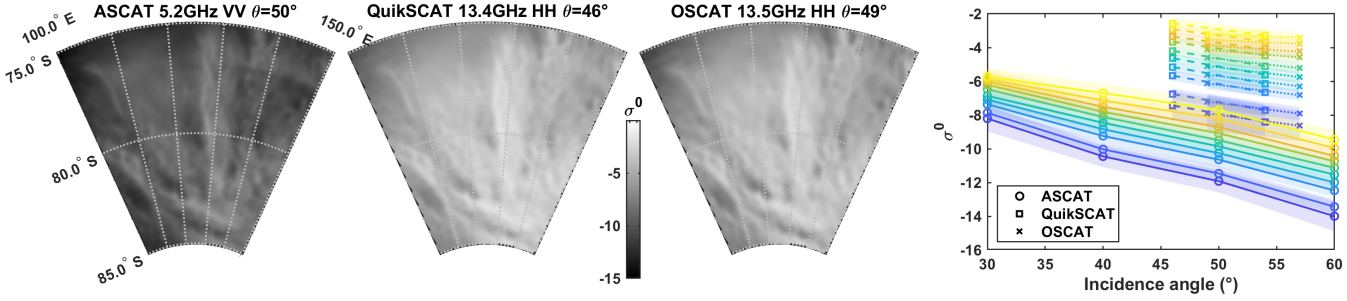

Figure 3. Visualization of the scatterometry datasets : ASCAT (5.2 GHz), QuikSCAT (13.4 GHz), and OSCAT (13.5 GHz). The plot on the right shows the dependence with incidence angle for all three datasets, using the same clusters and colors as in Fig. 2. Note also that OSCAT and QuikSCAT are in HH polarization at the smaller incidence angles (46°and 49°, respectively) and VV at the larger incidence angles (54°and 57°), as detailed in Table 1.

probed at several frequencies considered herein (Table 2), the Antarctic snowpack densities lie around $450-550\,\mathrm{kg.m^{-3}}$, which is intermediate between snow and ice. However, most common scattering models, such as the improved Born approximation (IBA) or the dense-media radiative transfer quasi-crystalline approximation (DMRT-QCA), become inaccurate within this intermediate range, with a discontinuity between snow and ice (Picard et al., 2022a). The symmetrized version of the strong contrast expansion addresses this issue.

To solve the radiative transfer equation we selected the the Discrete Ordinate (DORT) method (Picard et al., 2022b) which offers a consistent solution for both the active and passive mode.

The snow microstructure model used for each layer is the scaled exponential as modified in Picard et al. (2022a) with a polydispersity of $K = 0.62$ found to be suitable in Antarctica. The model outputs the H- and V-polarized brightness temperature T_B in K at each AMSR2 frequency, as well as the HH- and/or VV- polarized ASCAT, QuikSCAT, and OSCAT normalized radar cross-sections σ^0 at the frequencies and incidence angles of these instruments (see Table 1).

3.2 Snowpack model and parameters

Our snowpack model assumes continuous variations of grain size and density with depth. Field measurements have shown that models with continuously increasing density and grain size fit reasonably well the observed behaviors (Albert et al., 2004; Courville et al., 2007; Brucker et al., 2010; Picard et al., 2014; Leduc-Leballeur et al., 2015; Inoue et al., 2024). However, these models do not account for the random variations around these behavior, caused by seasonal and regional variations in precipitation, wind, and temperature and especially important in the top few meters. Rather than identifying a realistic snow profile corresponding to field measurements, as previously done by e.g. Picard et al. (2022b), we are attempting to fit general behaviors in grain size and density over large regions. We therefore assume that random and unresolved fluctuations do not significantly affect the microwave observations presented in Section 2 (Brucker et al., 2010; Leduc-Leballeur et al., 2015). The assumption of continuous variations in grain size and density is less valid in H polarization, which is sensitive to

https://doi.org/10.5194/egusphere-2024-3972
Preprint. Discussion started: 20 March 2025

Frequency (GHz)	5.2	6.9	10.65	13.4	13.5	18.7	36.5	89.0
Maximum probed depths (m)	22–88	22–102	9.4–39	2.8–11	2.7–11	2.6–11	0.4–3.4	0.1–0.7

Table 2. Estimated maximum depths probed at each frequency, calculated following Section 3.2. The range of values corresponds to the range of snowpack parameters given in Table 3. The depth is divided by 2 for frequencies corresponding to radar instruments (5.2, 13.4, and 13.5 GHz) to account for 2-way travel through the snowpack.

horizontal structures such as layers, and for high-frequency radiometry. The 89 GHz radiometry especially, which probes down to centimetric depths (Picard et al., 2012), is very sensitive both to temperature variations and to the presence of an ice crust in the wind-glazed regions.

We simulate a 10-layer snowpack, with or without the presence of a thin, uniform ice crust on top. The maximum depth is chosen to be 200 m, at which the snowpack has always densified to solid ice (Hörhold et al., 2011; Leduc-Leballeur et al., 2015). The dielectric properties of the substrate follow the default SMRT framework, which follows (Matzler et al., 2006, p. 456–461) and are valid for the frequency range of 0.01-3000 GHz and ice temperatures of 20-273.15 K; the same model has been used on Jupiter's icy moons by Brown et al. (2023). Within the framework of the SMRT model with the exponential microstructure, each layer is characterized by four parameters: layer thickness, temperature, density, and correlation length.

Layer thickness: The SMRT model, which does not account for coherent effects, imposes that every layer must be thicker than $\lambda/4$, which for the lowest frequency (5.2 GHz; ASCAT) is 1.44 cm. Using the extreme low and high values of each parameter described above and in Table 3, we estimate the depths probed by each frequency. The maximum depth probed is calculated as the depth z_i beyond which the optical depth of the above layers $\int_0^{z_i} \tau(z)dz$ is > 2; beyond this point, the structure of the snowpack does not significantly affect the signal at a given frequency. The optical depth of a given layer is calculated as $\tau = \kappa_e \times dz$, where $\kappa_e = \kappa_a + \kappa_s$ is the power extinction coefficient accounting for losses due to both absorption (κ_a)and scattering (κ_s), provided for each layer as an SMRT output, and dz is the layer thickness. The resulting maximum probed depths for the full range of parameters are provided in Table 2. Note that the minimum values of these depths correspond to large grain sizes leading to very high scattering (κ_s dominates) whereas the highest values correspond to small grain sizes and very low scattering (κ_a dominates). To fully sample the depths probed by each frequency, we chose 10 layers at exponentially increasing depths from 2 cm to 100 meters. Increasing the number of layers has no effect on the resulting emissivities and σ^0, indicating that the chosen sampling is sufficient. The bottom of the snowpack is modeled as a semi-infinite solid ice with density $917\ \mathrm{kg.m^{-3}}$ and grain size identical to that at 100 m depth.

Layer temperature: Because the microwave radiometry is averaged over a full year, we assume that the temperature is constant with depth, at least down to the depths probed at these frequencies. The temperatures are varied between -40 and -50°C. These values are typical of the region of interest, although they do not encompass the full range of annually averaged temperatures (-34° to -53°). Because we find that temperature influences both emissivities and backscatter values very little (Section 4), we do not test more values herein.

https://doi.org/10.5194/egusphere-2024-3972
Preprint. Discussion started: 20 March 2025

Layer density: The density variation with depth follows a simple exponential model reaching the value for solid water ice at depth (Bingham & Drinkwater, 2000; Leduc-Leballeur et al., 2015):

$$\rho(z) = \rho_{ice} - (\rho_{ice} - \rho_{top})e^{-Bz} \tag{1}$$

where $\rho_{ice} = 917\ \mathrm{kg.m^{-3}}$ is the density of water ice, ρ_{top} is the value at the surface, and B is an empirical value in $\mathrm{m^{-1}}$, whose value depends on the snow type (Bingham & Drinkwater, 2000). Leduc-Leballeur et al. (2015) find $B = 0.017\ \mathrm{m^{-1}}$ at Dome C in Antarctica. This density profile matches well those found in Antarctic firn regions with low accumulation, where the pore close-off occurs deeper than is typical elsewhere (Van Den Broeke, 2008; Hörhold et al., 2011; Leduc-Leballeur et al., 2015).

Layer correlation length: Previous work has found that, for the grain sizes used in microwave radiometry simulations to be comparable to the optical grain size measured in the field, a corrective factor must be used (e.g. the stickiness). Recently, Picard et al. (2022a) has identified this factor as the polydispersity K, an intrinsic property of the snow microstructure, which can be measured from e.g. micro-computed tomography (Coléou et al., 2001). To use the correct value as correlation length, we use the microwave grain size, defined by Picard et al. (2022a) as:

$$l_{MW} = K \times l_P \tag{2}$$

where l_P is the Porod length, calculated from the layer density ρ, ice density $\rho_{ice} = 917\ \mathrm{kg/m^3}$ and optical grain radius r_{opt} as follows (Picard et al., 2022b):

$$l_c = 4/3(1 - \rho/\rho_{ice})r_{opt} \tag{3}$$

By comparing AMSR2 observations to SMRT simulations in a region where the vertical structure of the snowpack had been measured, Picard et al. (2022a) found that the best value for K for Antarctic snow is 0.62. We therefore use this value herein, making the optical grain size r_{opt} directly comparable to field measurements but this does not affect our results as fitting l_p or l_{MW} given a constant K is equivalent.

We model the increase of optical grain radius r_{opt} with depth z as follows (Brucker et al., 2010; Bingham & Drinkwater, 2000):

$$r_{opt}^n(z) = r_{top}^n + Q_n z \tag{4}$$

where r_{top} is the grain radius at the surface in m, Q_n is the snow grain-size gradient in $\mathrm{m^n m^{-1}}$, and n is the growth exponent. This model assumes a linear increase in grain radius ($n = 1$), surface ($n = 2$), or volume ($n = 3$) with time from metamorphism, and therefore with depth assuming that snow accumulation is constant. It was shown by Brucker et al. (2010) to reproduce well the emissivities at 19 and 37 GHz within the Antarctic snow cover, and to be consistent with relative grain sizes over different regions of Antarctica.

Surface ice crust: The wind-glazed regions are covered by an ice crust formed by snow ablation from wind and sublimation (Courville et al., 2007). The thickness of this crust is likely millimetric, but there are other similarly thin ice layers embedded

https://doi.org/10.5194/egusphere-2024-3972
Preprint. Discussion started: 20 March 2025

Parameter	Symbol	Unit	Values	Reference
Ice crust thickness	z_{crust}	mm	0 (no crust) to 10	Albert et al. (2004); Courville et al. (2007)
Surface density	ρ_{top}	$\mathrm{kg.m^{-3}}$	300 to 450	Albert et al. (2004); Leduc-Leballeur et al. (2015)
Surface grain radius	r_{top}	mm	0.1 to 0.5	Courville et al. (2007); Brucker et al. (2010)
Density exponent factor	B	$\mathrm{m^{-1}}$	0.016 to 0.017	Bingham & Drinkwater (2000); Leduc-Leballeur et al. (2015)
Snow grain-size gradient	Q_1	$\mathrm{mm.m^{-1}}$	0.005 to 0.1	
	Q_2	$\mathrm{mm^2.m^{-1}}$	0.02 to 0.1	Brucker et al. (2010)
	Q_3	$\mathrm{mm^3.m^{-1}}$	0.01 to 0.1	
Temperature	T	°C	-40 to -50	Picard et al. (2022a)
Polydispersity	K		0.62	Picard et al. (2022a)

Table 3. Snowpack parameters for Antarctica SMRT simulations

within the top few meters of the snowpack (Albert et al., 2004). Exact simulation of the thickness or depth of these ice layers is irrelevant because it is highly variable over the 12.5 km resolution used herein. We therefore model the ice crust as a single high-density ($917\ \mathrm{kg.m^{-3}}$) ice layer on top of the snowpack, of thickness varying from 1 to 10 mm. Some of these thicknesses are smaller than $\lambda/4$ for ASCAT waves and the longest AMSR2 wavelengths. The SMRT can accomodate a single layer thinner than $\lambda/4$ by calculating explicitly the coherent effect through this layer following Montpetit et al. (2013); Proksch et al. (2015). This is implemented by setting the option *process_coherent_layer=True*, but can only process coherent scattering due to the layer thickness, not due to grain size.

The simulated snowpack therefore has six parameters, summarized in Table 3. The resulting depth and density profiles are shown in Fig. 4.

The SMRT model outputs the simulated brightness temperature T_B at each AMSR2 frequency in H and V polarizations. The emissivity is found by dividing the simulated T_B by the assumed snowpack temperature. The model also outputs the simulated normalized radar cross-section σ^0 at each sensed polarization and incidence angle for QuikSCAT and OSCAT (see Table 1), and for ASCAT in VV polarization at incidence angles of 30°, 40°, 50°, and 60°.

4 Results and interpretation

4.1 Uniform density or grain size

We first tested the model with either density or grain size uniform with depth, while the other of the two varies as described above (Section 3.2). The result of the simulation for AMSR2 V-polarized emissivities is shown in Fig. 5 for physically reasonable values of the parameters; other values only lead to worse fits. As shown in this figure, the model is unable to simultaneously fit all AMSR2 frequencies if either the grain size or the density are kept constant.

Attempting to reproduce the observations with either the density or the grain size uniform with depth is unsuccessful. If the grain size is kept uniform, then we generally find excessive scattering (low emissivities) at high frequencies and insufficient

https://doi.org/10.5194/egusphere-2024-3972
Preprint. Discussion started: 20 March 2025

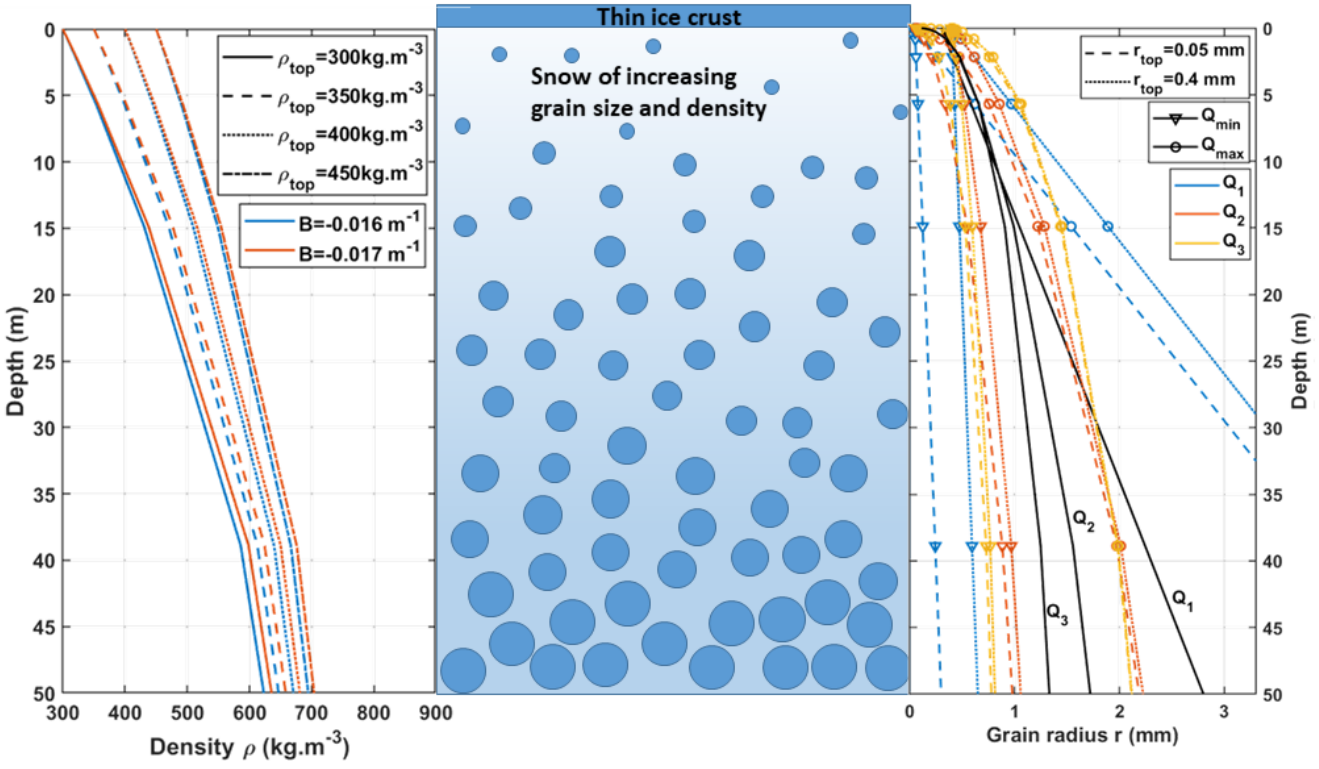

Figure 4. Schematic representation of the modeled snowpack, with (left) the density and (right) the grain radius variations with depth. Different line patterns correspond to different parameter values. The snow grains are shown here as circles for simplicity, but are not spherical neither in reality nor in the model; the complex grain shape is accounted for by the polydispersity K. On the grain radius plot, the profiles which reproduce the best the simulations are shown for Q_1, Q_2, and Q_3 in black; note that these three profiles are very similar in the top 15 meters, to which the observations are most sensitive.

scattering (high emissivities) at low frequencies (Fig. 5, left). This demonstrates that grain size must increase with depth to fit the observed spectra. The increase in grain size with depth in the Antarctica snowpack, as well as its influence on microwave emissivities, have long been known (e.g. Jay Zwally, 1977; Brucker et al., 2010). If instead the density is kept uniform, the simulated emissivities as a function of frequency have a concave shape, whereas a convex one is expected: the lowest and highest frequencies appear to scatter excessively (Fig. 5, right). This would not occur if the density was not constant, consistent with increasing density with depth and a likely crusted surface affecting the 89 GHz values.

Brucker et al. (2010) modeled the Antarctic snowpack at 19.3 and 37 GHz with increasing grain size but constant density and found a reasonable match to the data (i.e. a roughly flat emissivity spectrum). We are also able to reproduce the data with the same model within this range, although with different values for the parameters r_{top} (we find $r_{top} \approx 0.2$ mm; they find $0.45 < r_{top} < 0.65$ mm) and Q_2 (we find $Q_2 \approx 60000\ \mu\text{m}^2.\text{m}^{-1}$; they find $400000 < Q_2 < 820000\ \mu\text{m}^2.\text{m}^{-1}$) . This discrepancy is due to modeling differences between our simulations and those of Brucker et al. (2010). They used the DMRT-ML

https://doi.org/10.5194/egusphere-2024-3972
Preprint. Discussion started: 20 March 2025

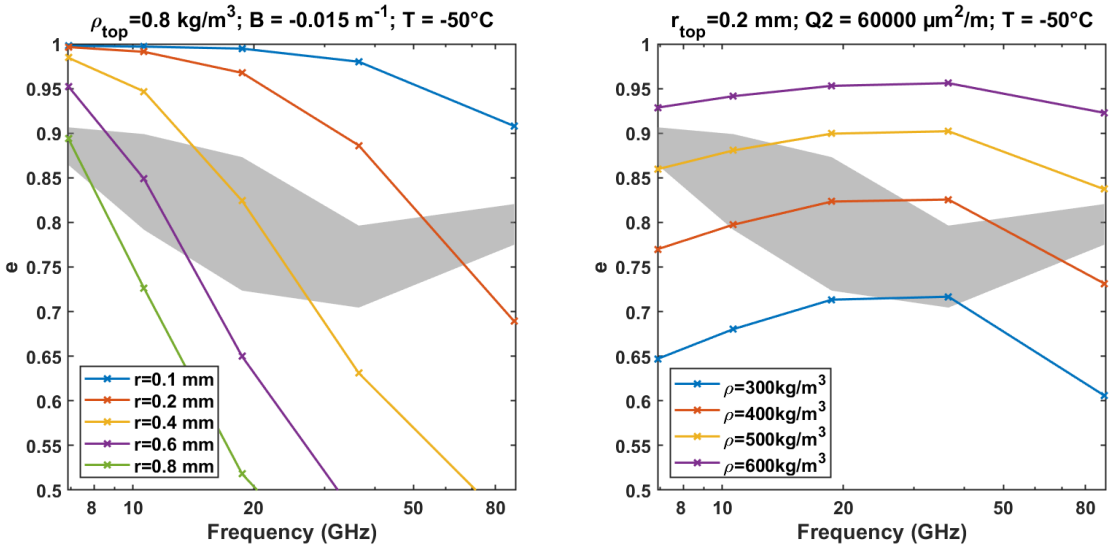

Figure 5. AMSR2 V-polarized emissivities simulated by the SMRT for a snowpack with either (left) uniform grain size with depth or (right) uniform density with depth. The grayed region shows the full range of observed values within the ROI. The parameter values used for each simulation are indicated in the title.

model composed of spheres, whereas we use the SymSCE model while accounting for polydispersity (as defined by Picard et al. (2022b)). In any case, we show that while assuming constant density can be reasonable at 19.3 to 37 GHz, it is inconsistent with observations over a wider spectrum range.

4.2 Variable density and grain size, without an ice crust

We then vary simultaneously the grain size and the density with depth, as described in Section 3.2, but without any icy crust at the surface. We are not attempting to fit the model to the data, but instead to simulate the correct range of values for several different datasets with a snowpack model as simple as possible. For simplicity, we only show in Fig. 6 the combination of parameters which best match the observations, for linear (Q_1), square (Q_2), and cubic (Q_3) increase in grain size with depth. We plot emissivity in each polarization e_V and e_H versus frequency and σ^0 versus incidence angle in C-band (ASCAT) and in Ku-band (QuikSCAT and OSCAT).

We find that all considered microwave active and passive observations except H-polarized emissivities can be simultaneously simulated by the SMRT for reasonable values of the parameters. A summarized analysis of the influence of each parameter is given below.

Within the ranges expected in the Antarctic megadunes region, the snowpack **temperature** T and the **density e-folding factor** B have very little influence on both the emissivities and the σ^0 values ($\Delta e < 0.05$ and $\Delta\sigma^0 < 0.6$ dB). To simplify the visualization, simulated values are shown only for $B = -0.017$, the value deduced from fitting two 80-m-long density profiles

https://doi.org/10.5194/egusphere-2024-3972
Preprint. Discussion started: 20 March 2025

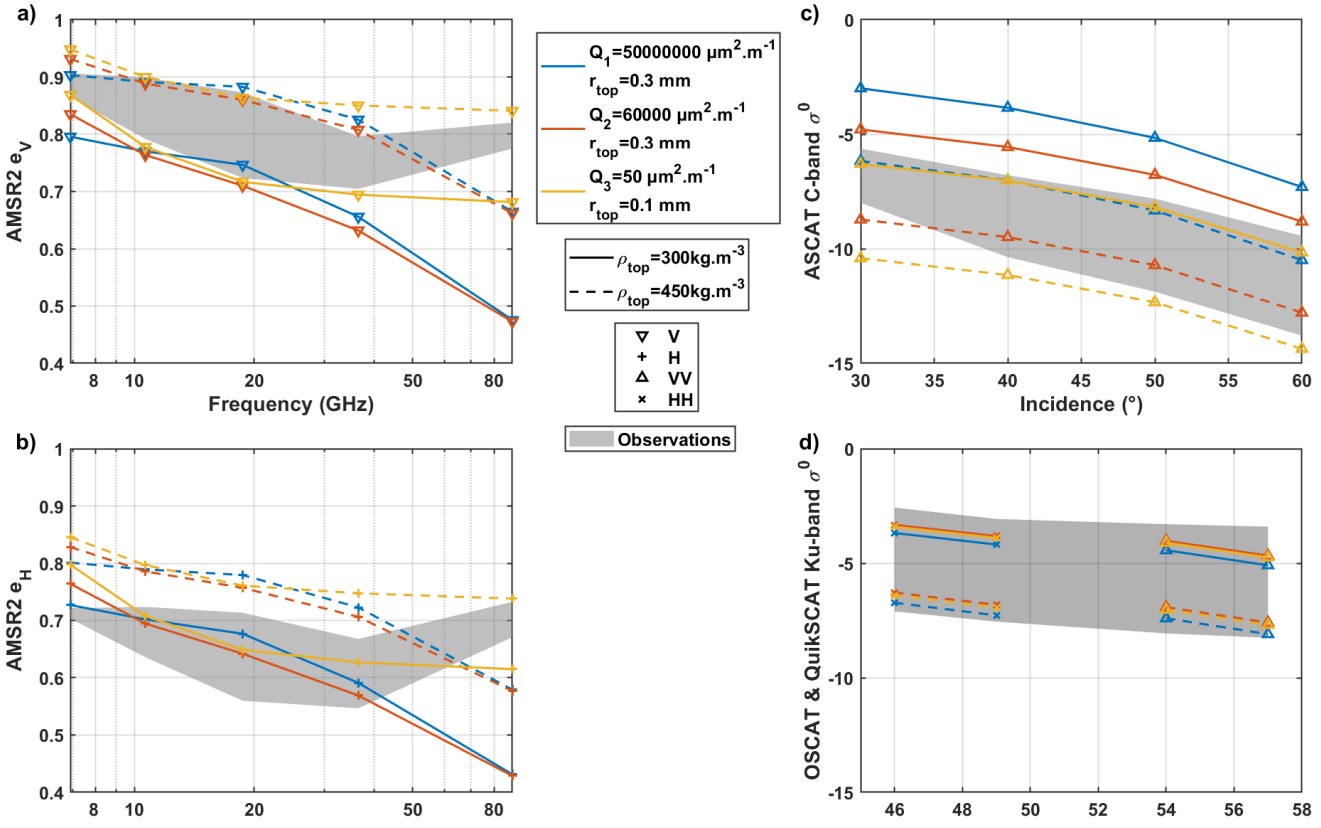

Figure 6. Best fitting simulations of AMSR2 V-polarized (a) and H-polarized (b) emissivity spectra and C-band ASCAT (c) and Ku-band QuikSCAT and OSCAT (d) backscatter σ^0 for different surface densities ρ_{top} and grain size profiles (gradient Q_n and surface grain radius r_{top}), while fixing the temperature $T = -50\,^{\circ}\mathrm{C}$ and density e-folding factor $B = 0.017\ \mathrm{m}^{-1}$. For each set of data, the range of observations is shaded in gray. For simplicity, only the minimum and maximum values of density tested are shown: varying the surface density therefore corresponds to the space between the two lines of a given color. The range between the yellow lines (for Q_3) thus results in good fits for all except H-polarized data.

https://doi.org/10.5194/egusphere-2024-3972
Preprint. Discussion started: 20 March 2025

at dome C by Leduc-Leballeur et al. (2015), and $T = -50°$C, the annual mean temperature measured by Picard et al. (2022b) in the Antarctic megadunes.

The **grain size**, defined by the parameters r_{top} and Q_n, is the primary control on the shape of the microwave emissivity spectrum. The surface grain size r_{top} affects high frequencies (which probe shallower depths) the most, whereas Q_n controls the grain size profile with depth and therefore influences lower frequencies. Assuming a linear increase of grain size with depth (Q_1) leads to high grain sizes at depth and small at the surface; ASCAT data, which is at lower frequency than 10–89 GHz AMSR2 and therefore probes deeper, can never be reproduced for the same configuration as AMSR2 data. Meanwhile, all data except H-polarized emissivities can be simulated with a cubic increase with depth (Q_3), while the square option (Q_2) also has difficulties with the 89 GHz data (see Fig. 6). As found by Brucker et al. (2010), we can thus exclude the case $n = 1$, but both other options are acceptable approximations: grain size in the subsurface is probably a more complex function of precipitation rates, temperature, and random variations. The grain radii we find in the subsurface are very large, with values around 1 mm at 15 m depths. Since the concept of grain size can be approached in many different ways (e.g., Picard et al., 2022b), we do not speculate on the subsurface grain size.

The **surface density** ρ_{top} affects the backscatter and emissivity at all frequencies almost equally (Fig. 6). The density controls the effective dielectric constant of the medium, and therefore strongly affects the probed depths (with a denser medium being less transparent). Thus, to first order, the lower the density, the larger the path length within the medium, and the more opportunities for multiple subsurface scattering, leading to lower emissivities and higher σ^0. Scattering also varies in a complex manner with density (figure 2 of Picard et al. (2022a)); however, in our case this effect is difficult to disentangle from that of grain size, since both properties vary simultaneously with depth.

We find that the **H-polarized AMSR2 emissivities**, shown in Fig. 6b, are poorly reproduced by the parameters that match the rest of the data best, and would require higher grain sizes (r_{top} and/or Q_2) than the V-polarized emissivities. This is likely due to the polarization properties of the medium, caused by layers of varying density (embedded thin ice layers) and by a surface crust. Indeed, ice layers remain mostly invisible to V-polarized radiation near the Brewster angle, whereas H-polarized radiation is very sensitive to these vertical dielectric contrasts (Leduc-Leballeur et al., 2015).

The simulated **89 GHz emissivity** ($\lambda = 3.34$ mm) in V polarization is often very low, especially for surface grain sizes $r_{top} \geq 0.2$ mm. These large grains (compared to the wavelength) cause very important simulated scattering at 89 GHz. The $n = 3$ option allows to start with very low grain size at the surface and increase quickly with depth; yet even so, the 89-37 GHz slope is never reproduced (Fig. 6). At the depths probed at 89 GHz (a few centimeters), the simulated snowpack is in fact not realistic. Indeed, it does not account for the observed ice crust in the wind-glazed regions, the variations of temperature with depth and season, and the random variations of density and grain size at these depths.

4.3 With an ice crust

To attempt to fit the H-polarized AMSR2 emissivities and the 89 GHz V-polarized AMSR2 emissivities, we add an ice crust of variable thickness on top of the snowpack. Such an ice crust is common within the wind-glazed regions and is likely to polarize the outgoing signal, decreasing H-polarized emissivities. The results of these simulations are shown for e_V, e_H , C-band σ^0,

https://doi.org/10.5194/egusphere-2024-3972
Preprint. Discussion started: 20 March 2025

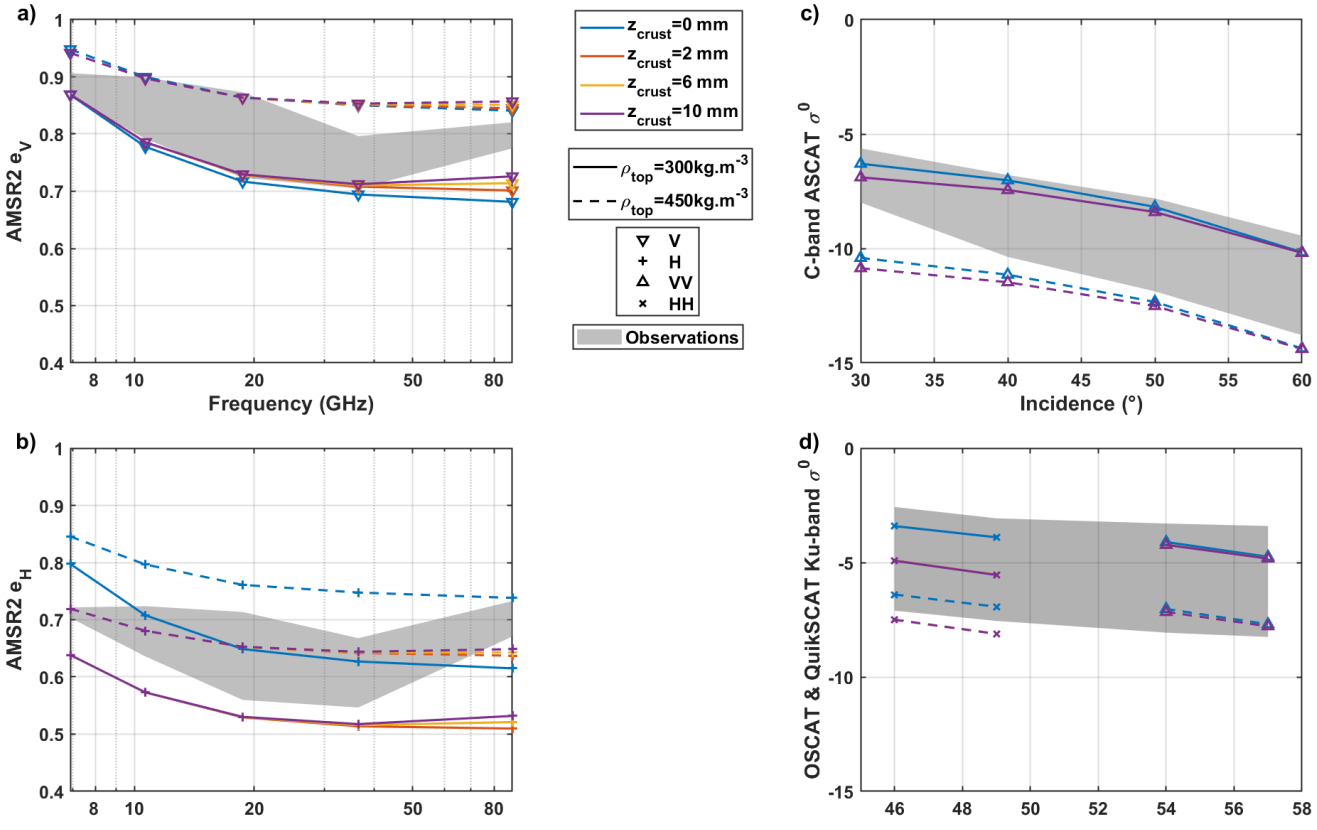

Figure 7. AMSR2 V-polarized (a) and H-polarized (b) emissivity spectra and C-band ASCAT (c) and Ku-band QuikSCAT and OSCAT (d) backscatter σ^0 for different values of the surface density ρ_{top} and ice crust thickness z_{crust} while fixing the surface grain radius $r_{top} = 0.1$ mm , grain-size gradient $Q_3 = 50\ \mu\text{m}^3.\text{m}^{-1}$, temperature $T = -50\ ^\circ\text{C}$, and density e-folding factor $B = 0.017\ \text{m}^{-1}$. As in previous plots, the full range of observed emissivities and backscatter values within the region of interest is shaded in gray. The simulated scatterometry is identical for $z_{crust} = 2, 6$, or 10 mm, and overlap in c) and d). Note that, for $z_{crust} = 0$ (no crust), the simulated values are the same as highlighted in green in the previous section.

and Ku-band σ^0 (Fig. 7), for $T = -50°\text{C}$ $B = -0.017\ \text{m}^{-1}$, $r_{top} = 0.1$ mm, and $Q_3 = 50\ \mu\text{m}^3.\text{m}^{-1}$. These parameter values, which reproduce reasonably well the expected σ^0 and e_V without an ice crust, were chosen for the figure, but the effect of the ice crust is similar for all other tested parameter combinations.

V polarized emissivities e_V: As shown in Fig. 7a, an ice crust ≤ 1 cm thick can change the 89 GHz emissivities by at most 0.04, and remains insufficient to explain the observed 37-89 GHz slope. A thicker crust might be able to reproduce the observations, but would not be realistic: the thickness of the ice crust and underlying ice layers observed in the field is of the order of millimeters, not centimeters. Here, our simplified model seems insufficient, and it may be necessary to add complexity

https://doi.org/10.5194/egusphere-2024-3972
Preprint. Discussion started: 20 March 2025

such as superimposed layers of randomly varying density to improve the fit. At 89 GHz, radiometry is also very sensitive to surface temperature, which is seasonally much more variable than the temperature at depth.

H polarized emissivities e_H: Comparing the emissivity spectra for $z_{crust} = 0$ (no ice crust) with the others (all identical below 37 GHz), Fig. 7b shows that the polarization induced by the ice crust decreases e_H. This decrease is sufficient, and even slightly in excess, to reproduce the H-polarized observations. This is true regardless of the thickness of the ice crust, because the air-surface interface, which controls the H polarization, is the same.

Scatterometry σ^0: The ice crust decreases the simulated QuikSCAT and OSCAT backscatter in HH polarization, but does not affect the VV-polarized scatterometry (Fig. 7c and d). Regardless of the crust thickness, the effect on the HH-polarization is so strong in the simulations that σ^0 is predicted to be lower at 46° and 49° incidence in HH than at 54° and 57° in VV. This does not match the OSCAT and QuikSCAT observations, which show σ^0 decreasing with incidence angle regardless of the polarization (Fig. 3). This could perhaps be explained by the presence of surface roughness, regional heterogeneity within the 12.5 km pixels, or coherent scattering, which can affect the polarization ratio of active data (Hofgartner & Hand, 2023).

Including a thin ice crust in SMRT simulations helps lower the H-polarized emissivities, but is insufficient to explain the 89 GHz e_V and e_H, and even introduces new discrepancies to the H-polarized scatterometry. Thus, a simple snowpack model is sufficient to reproduce the 6.9–37 GHz e_V and 5.2–13.5 GHz σ^0, but more complexity must be introduced for higher frequencies and for H polarization. This complexity can include a thin ice layer as tested here, but also a time- and depth-varying temperature profile, random layer densities and grain sizes, a different grain size gradient in the top few centimeters, or surface roughness. While this result illustrates the limits of a simple snowpack model, it also highlights the richness of these complementary datasets, which used in synergy can provide constraints on subsurface properties inaccessible from one frequency, polarization, or mode alone.

5 Discussion

5.1 Wind-glazed regions of Antarctica as an analog for Saturn's icy moons

The Antarctic wind-glazed regions are an excellent analog for microwave observations of icy moons. Their very low temperatures year-round do not allow melting of the snow and ice (Traversa et al., 2023). The high purity of the water ice, due to the distance to both sea and rocky outcrops, is also analogous to icy moons, especially Enceladus (e.g., Le Gall et al., 2023). The very low precipitation rates and near-zero snow accumulation (Traversa et al., 2023) may be as close as we can get to atmosphere-less lunar environments with almost no external material brought to the surface, and allow the development of structures stable for years. Another advantage of studying this region is the large amount of available satellite observations and the few in-situ campaigns in these regions, providing strong constraints to test the modeling approach before its application to more uncertain conditions on icy moons.

Yet, like all Earth analogs for other planetary surfaces, this one is also imperfect. The temperature remains much higher than in the outer solar system, where airless bodies can also witness large surface temperature variations (e.g., between 40 and 140 K for Saturn's moons, Howett et al., 2010). The higher Earth temperatures lead to faster sublimation and development of depth

https://doi.org/10.5194/egusphere-2024-3972
Preprint. Discussion started: 20 March 2025

hoar, as well as slightly different dielectric properties and higher absorption losses: microwaves can probe considerably deeper in colder ice. The second major difference is the presence of an atmosphere, with important katabatic winds (Scambos et al., 2012) and occasional precipitation. Meanwhile, icy moons are airless but are affected by exogenic processes, including impact gardening and electron bombardment, likely causing differences in the surface structure (crystal size, presence of a crust, depth of regolith...), which remains poorly understood on icy moons.

The introduction of a new icy moon analog is encouraging for further work analyzing the microwave properties of icy moons. It could be used to examine the role of coherent backscatter in Earth snow (Stefko et al., 2022) or the variations of microwave signals with the presence of non-icy material even in small quantities, which has been observed on icy moons (Le Gall et al., 2019, 2023).

5.2 Implications for Saturn's icy moons

We have seen that the SMRT is able to successfully simulate simultaneously active and passive Ku-band observations in the Antarctica megadunes region (Section 4). Our main objective now is to check if a simple configuration of the SMRT is also able to reproduce at the same time the Ku-band radiometry and radar observations of Saturn's mid-sized icy moons Mimas, Enceladus, Tethys, Dione, Rhea, Iapetus, and Phoebe by the Cassini Radar (Le Gall et al., 2019, 2023). We therefore chose a simple two-layer model of regolith (modeled as snow in the SMRT) on top of ice, with a constant temperature profile, at the Cassini Radar frequency (13.78 GHz), and with the default dielectric properties from Matzler et al. (2006). There are thus six parameters as shown in Table 4: the density and grain radius of each layer, the thickness of the regolith, and the temperature. Given the large uncertainties and likely large inter- and intra-satellite variations in the density, grain size, composition, and structure of icy moon regoliths, each parameter is left to vary within a very large range.

The regolith of icy moons at meter depths is poorly understood, with some parameters entirely unconstrained. Measured surface porosities vary depending on the satellite, model, and data from 0.05 to 0.99 (Carvano et al., 2007, and references therein), but generally need to be very high to match near to far infrared observations (Carvano et al., 2007; Ciarniello et al., 2011; Ito et al., 2022). Compaction due to gravity is insignificant for hundreds of meters to tens of kilometers of depth, especially on Saturn's mid-sized moons (Mergny & Schmidt, 2024), but other processes such as cryovolcanic or tectonic activity, impacts, radiation, or sintering could affect both density and grain size (Molaro et al., 2019). Grain size is similarly poorly constrained, with surface values measured between $1\ \mu\mathrm{m}$ (Ito et al., 2022), tens of $\mu\mathrm{m}$, and up to $200\ \mu\mathrm{m}$ in the Enceladus South polar terrain (Jaumann et al., 2008; Taffin et al., 2012); subsurface values remain unknown. Grain radii beyond 1 mm are possible, but are not simulated herein due to the transition to a Mie scattering regime, which is not included in the SMRT model. Grain radii below $50\ \mu\mathrm{m}$ are too small to significantly affect the scattering at 2.2 cm wavelength, so are not tested in the model. The temperature can vary from about 40 to 140 K at the surface (Howett et al., 2010), but is less extreme in the subsurface probed by microwaves (Bonnefoy et al., 2020; Le Gall et al., 2023): we therefore chose a range of 60 to 120 K, which is still very wide. Finally, the thickness of the porous regolith is generally assumed to be of the order of meters (Bland et al., 2015; Ries & Janssen, 2015), but is of the order of hundreds of meters at least near the pit chains of Enceladus (Martin et al., 2023). These various observations justify the large parameter ranges shown in Table 4. Meanwhile, polydispersity is

https://doi.org/10.5194/egusphere-2024-3972
Preprint. Discussion started: 20 March 2025

Parameter	Symbol	Unit	Values	Comments and reference
Regolith grain radius	r_{top}	mm	0.05 to 1	Jaumann et al. (2008); Taffin et al. (2012); Ito et al. (2022)
Regolith density	ρ_{top}	$\mathrm{kg.m^{-3}}$	10 to 450	Carvano et al. (2007); Ciarniello et al. (2011); Ito et al. (2022)
Ice grain radius	r_{ice}	mm	0.05 to 1	
Ice density	ρ_{ice}	$\mathrm{kg.m^{-3}}$	500 to 900	
Regolith thickness	Z_{top}	m	1 to 1000	Bland et al. (2015); Martin et al. (2023)
Temperature	T	K	60 to 120	Howett et al. (2010); Le Gall et al. (2023)
Polydispersity	K		0.62	

Table 4. Snowpack parameters for icy moon SMRT simulations

assumed to be the same as in Antarctica. Grain radii are kept below 1 mm because beyond that value, Mie scattering, which is not accounted for the SMRT, becomes significant in Ku band (2.2 cm for the Cassini Radar).

Most observations of the icy moons by the Cassini Radar/radiometer were not resolved, and included multiple incidence angles simultaneously. We therefore request the SMRT to output the NRCS σ^0 and the brightness temperature T_B in both polarizations (H and V for radiometry; HH and VV for radar) and for all incidence angles with a step of 5°. Emissivities e_V and e_H are calculated by dividing the brightness temperature by the assumed medium temperature T. Both σ^0 and e are then integrated over the disk (only in same-sense-linear polarization for σ^0), following Wye et al. (2007) and Le Gall et al. (2019) while also accounting for both polarizations:

$$A_{SL}^{disk} = \int_0^{\pi/2}\int_0^{2\pi} (\sigma^0_{VV}(\theta,\phi)\cos^2\phi + \sigma^0_{HH}(\theta,\phi)\sin^2\phi)\sin\theta d\phi d\theta/\pi \tag{5}$$

$$e^{disk} = \int_0^{\pi/2}\int_0^{2\pi} (e_V(\theta,\phi)\cos^2\phi + e_H(\theta,\phi)\sin^2\phi)\sin\theta\cos\theta d\phi d\theta/\pi \tag{6}$$

The resulting disk-integrated values are then directly comparable to those observed by the Cassini Radar/radiometer and examined by Le Gall et al. (2023). For comparison, we also simulate equivalent disk-integrated observations for the Antarctica megadunes region. Using the same SMRT configuration as in Section 3 with our best-fitting parameters ($T = -50$°C, $B = -0.017$ $\mathrm{m^{-1}}$, $r_{top} = 0.3$ mm, $Q_2 = 100000$ $\mu\mathrm{m.m^{-1}}$, and 300 $\mathrm{g.m^{-3}} < \rho_{top} < 450$ $\mathrm{g.m^{-3}}$), we simulate Ku-band observations at all incidence angles and calculate A_{SL}^{disk} and e^{disk} as above.

Plotting all disk-integrated values simulated by the SMRT regardless of the parameters over the Jupiter and Saturn moon observations from Le Gall et al. (2023) shows that the model can reproduce observations of Jupiter's icy moons, but never of Saturn's moons, which remain too radar-bright (Fig. 8) . This is likely because the model simulates only incoherent scattering, whereas the coherent backscatter opposition effect (CBOE) has been hypothesized to be the main cause for icy moons unusual radar properties (Black, 2001; Le Gall et al., 2019, 2023; Hofgartner & Hand, 2023). The CBOE can at most multiply the

https://doi.org/10.5194/egusphere-2024-3972
Preprint. Discussion started: 20 March 2025

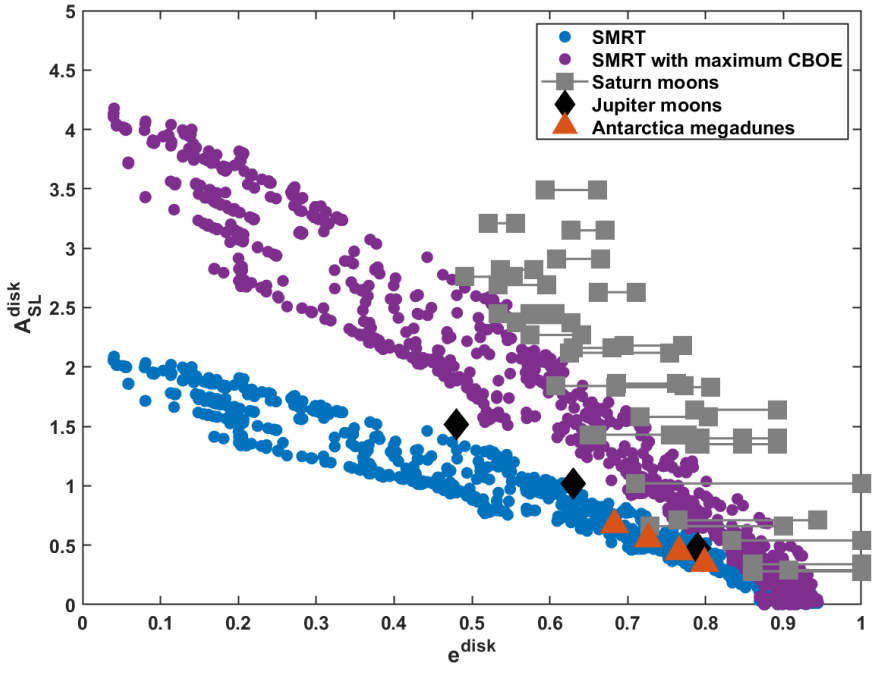

Figure 8. The results of SMRT simulations for a two-layer icy satellite model are shown, along with observations on Jupiter's and Saturn's icy satellites (from Le Gall et al., 2023) and simulated disk-integrated observations corresponding to the Antarctica megadunes region. Since the SMRT does not simulate the coherent backscatter opposition effect, A_{SL}^{disk} is multiplied by 2 to provide a maximum theoretical value; even so, the model is unable to reproduce most Cassini observations of Saturn's icy moons.

radar returns (σ^0 and therefore also A^{disk}) by a factor of 2. We plot SMRT simulations multiplied by 2, which correspond to maximum values, and find that these are consistent with some Saturn moon observations, but still insufficient for Enceladus, the radar-brightest object in the solar system.

6 Conclusions

We use the SMRT model to simulate AMSR2 6.9 to 89 GHz emissivities as well as C- and Ku-band scatterometry measured by ASCAT, OSCAT, and QuikSCAT in the Antarctic megadunes region. Modeling the Antarctic snowpack as layers with increasing density and grain size with depth allows us to reproduce simultaneously, for the first time, all V-polarized emissivities from 6.9 to 37 GHz and backscatter at 5.2 and 13.4 GHz. The observed microwave emissivity spectrum is slightly convex, but remains within the range $0.7 < e_V < 0.9$: this shape can only be explained with both density and grain size increasing with depth, which result from densification and metamorphism, respectively. Combining multiple frequencies thus provides insight

https://doi.org/10.5194/egusphere-2024-3972
Preprint. Discussion started: 20 March 2025

into the vertical profile, an approach which is also useful on icy satellites such as Iapetus (Bonnefoy et al., 2024) and Ganymede (Zhang et al., 2023; Brown et al., 2023), although variations in composition will also have to be considered.

The fact that 5–37 GHz Antarctica radar and radiometry data can be successfully simulated while ignoring coherent scattering, surface roughness, and random density and grain size fluctuations in the top few meters implies that both the active and passive V-polarized microwave signals at these frequencies are dominated by incoherent scattering on large subsurface grains. Meanwhile, to reproduce H-polarized emissivities, an ice crust over the snowpack is necessary, as observed in the wind-glazed regions; however it also reduces the HH-polarized scatterometry. This could likely be remedied by adding further complexity to the model, such as surface roughness which tends to moderate the polarization effect of flat interfaces. It is also possible that coherent scattering, either on large grains (Hapke, 1990) or caused by interference between layers (Leduc-Leballeur et al., 2015), plays a role in the scatterometry data. A strong difference between H and V (or HH and VV) is an indicator of a stratified snowpacks, or the presence of pure ice at the surface. Similarly, the observed 37–89 GHz slope in V- and H-polarized emissivities cannot be reproduced by the model, even when including a thin ice crust. A more realistic near-surface model appears to be required for the 89 GHz data, for instance with a seasonally varying temperature, or by modeling the strong gradient in grain size in the topmost 10-20 cm of the snowpack as observed in the field (Picard et al., 2022b).

The relative success of the simple snowpack representation and of the SMRT in reproducing 5–37 GHz active and passive microwave observations in the Antarctic megadunes region encourages its application to the radar and radiometry observations on icy moons, characterized by even higher scattering. A first application to icy moons using a wide range of parameters on a two-layer model is able to reproduce observations of Jupiter's moons. Meanwhile, to approach the observed radar and radiometry data on Saturn's moons, it is necessary to invoke coherent backscattering, consistent with previous work (Hofgartner & Hand, 2023). Even so, Saturn's satellites and especially Enceladus remain too radar-bright for the model configuration and range of parameters tested, hinting for example at very large grain sizes. The SMRT, with realistic hypotheses, thus significantly improves upon simulations by previous analytical models (Le Gall et al., 2023), but also highlights the importance of coherent scattering, which future work could incorporate into the model, for instance using the formulations of Markkanen & Penttilä (2023) or Muinonen & Penttilä (2024). CBOE is also likely on Earth (Stefko et al., 2022): successfully understanding, measuring, and modeling it will benefit both communities. It would also be interesting to attempt to reproduce resolved observations of Saturn's moons using more constraints such as resolved observations (Le Gall et al., 2014, 2017; Bonnefoy et al., 2020) or radiometry at multiple frequencies (Bonnefoy et al., 2024), for instance on Enceladus or Iapetus. Meanwhile, integrating non-icy components into the model may help understand both regional and satellite-to-satellite variations in microwave emissivity and radar brightness.

7 Environmentally responsible research

The work presented herein makes use of data from four Earth observation space missions: QuikSCAT, whose launch mass was 970 kg; ASCAT on the Metop-C satellite, whose launch mass was 3950 kg; OSCAT on Scatsat-1, whose launch mass was 377 kg; and AMSR2 aboard GCOM, whose launch mass was 2000 kg. Using a life-cycle emission factor of $50(\pm 10)$ $\mathrm{tCO2e.kg^{-1}}$

https://doi.org/10.5194/egusphere-2024-3972
Preprint. Discussion started: 20 March 2025

(Wilson, 2019; Knödlseder et al., 2022; Marc et al., 2024), these satellites have estimated carbon footprints of, respectively, $18,500$ tCO2e, $197,500$ tCO2e, $18,850$ tCO2e, and $100,000$ tCO2e, without accounting for other environmental impacts such as local pollution due to mining or ozone layer depletion caused by the launches. Since data from these satellites are not used only for research purposes but also for weather forecasting and private applications, it is difficult to estimate the impact per scientific paper. We also made use of data from the Cassini mission, which using the same method had an estimated carbon footprint of $392,902$ tCO2e, corresponding to 42 tCO2e per paper as of 2022 (Knödlseder et al., 2022). We wish to warn against unnecessary proliferation of infrastructures with such high environmental impact and instead promote sufficiency in both Earth and Planetary Science.

Acknowledgements. G.P. was supported by the French Polar Institute (IPEV) project number 1110.

https://doi.org/10.5194/egusphere-2024-3972
Preprint. Discussion started: 20 March 2025

References

Albert, M., Shuman, C., Courville, Z., et al. 2004, Annals of Glaciology, 39, 73, doi: 10.3189/172756404781814041

Bingham, A., & Drinkwater, M. 2000, IEEE Transactions on Geoscience and Remote Sensing, 38, 1810, doi: 10.1109/36.851765

Black, G. 2001, Icarus, 151, 160, doi: 10.1006/icar.2001.6615

Bland, M. T., McKinnon, W. B., & Schenk, P. M. 2015, Icarus, 260, 232, doi: 10.1016/j.icarus.2015.07.016

Bonnefoy, L. E., Le Gall, A., Lellouch, E., et al. 2020, Icarus, 352, 113947, doi: 10.1016/j.icarus.2020.113947

Bonnefoy, L. E., Lellouch, E., Le Gall, A., et al. 2024, Icarus, 115950, doi: https://doi.org/10.1016/j.icarus.2024.115950

Brodzik, M., Billingsley, B., Haran, T., Raup, B., & Savoie, M. 2014, ISPRS International Journal of Geo-Information, 3, 1154, doi: 10.3390/ijgi3031154

Brodzik, M. J., Billingsley, B., Haran, T., Raup, B., & Savoie, M. H. 2012, ISPRS International Journal of Geo-Information, 1, 32, doi: 10.3390/ijgi1010032

Brown, S., Zhang, Z., Bolton, S., et al. 2023, Journal of Geophysical Research: Planets, 128, e2022JE007609, doi: 10.1029/2022JE007609

Brucker, L., Picard, G., & Fily, M. 2010, Journal of Glaciology, 56, 514, doi: 10.3189/002214310792447806

Carvano, J., Migliorini, A., Barucci, A., & Segura, M. 2007, Icarus, 187, 574, doi: 10.1016/j.icarus.2006.09.008

Ciarniello, M., Capaccioni, F., Filacchione, G., et al. 2011, Icarus, 214, 541, doi: 10.1016/j.icarus.2011.05.010

Coléou, C., Lesaffre, B., Brzoska, J.-B., Ludwig, W., & Boller, E. 2001, Annals of Glaciology, 32, 75–81, doi: 10.3189/172756401781819418

Courville, Z. R., Albert, M. R., Fahnestock, M. A., Cathles, L. M., & Shuman, C. A. 2007, Journal of Geophysical Research, 112, F02030, doi: 10.1029/2005JF000429

Culberg, R., Schroeder, D. M., & Steinbrügge, G. 2022, Nature Communications, 13, 2007, doi: 10.1038/s41467-022-29458-3

Fahnestock, M. A., Scambos, T. A., Shuman, C. A., et al. 2000, Geophysical Research Letters, 27, 3719, doi: 10.1029/1999GL011248

Ferrari, C., & Lucas, A. 2016, Astronomy & Astrophysics, 588, A133, doi: 10.1051/0004-6361/201527625

Figa-Saldaña, J., Wilson, J. J., Attema, E., et al. 2002, Canadian Journal of Remote Sensing, 28, 404, doi: 10.5589/m02-035

Frezzotti, M., Gandolfi, S., Marca, F. L., & Urbini, S. 2002, Annals of Glaciology, 34, 81, doi: 10.3189/172756402781817851

Hapke, B. 1990, Icarus, 88, 407, doi: 10.1016/0019-1035(90)90091-M

Hill, J. C., & Long, D. G. 2017, IEEE Geoscience and Remote Sensing Letters, 14, 92, doi: 10.1109/LGRS.2016.2630010

Hobley, D. E. J., Moore, J. M., Howard, A. D., & Umurhan, O. M. 2018, Nature Geoscience, 11, 901, doi: 10.1038/s41561-018-0235-0

Hofgartner, J. D., & Hand, K. P. 2023, Nature Astronomy, doi: 10.1038/s41550-023-01920-2

Hörhold, M. W., Kipfstuhl, S., Wilhelms, F., Freitag, J., & Frenzel, A. 2011, Journal of Geophysical Research: Earth Surface, 116, n/a, doi: 10.1029/2009JF001630

Howett, C., Spencer, J., Hurford, T., Verbiscer, A., & Segura, M. 2016, Icarus, 272, 140, doi: 10.1016/j.icarus.2016.02.033

Howett, C., Spencer, J., Pearl, J., & Segura, M. 2010, Icarus, 206, 573, doi: 10.1016/j.icarus.2009.07.016

Inoue, R., Fujita, S., Kawamura, K., et al. 2024, The Cryosphere, 18, 425, doi: 10.5194/tc-18-425-2024

Ito, G., Kolokolova, L., Petrov, D., & Pitman, K. M. 2022, Journal of Quantitative Spectroscopy and Radiative Transfer, 291, 108320, doi: 10.1016/j.jqsrt.2022.108320

Janssen, M., Le Gall, A., & Wye, L. 2011, Icarus, 212, 321, doi: 10.1016/j.icarus.2010.11.026

Jaumann, R., Stephan, K., Hansen, G., et al. 2008, Icarus, 193, 407, doi: 10.1016/j.icarus.2007.09.013

Jay Zwally, H. 1977, Journal of Glaciology, 18, 195, doi: 10.3189/S0022143000021304

https://doi.org/10.5194/egusphere-2024-3972
Preprint. Discussion started: 20 March 2025

Knödlseder, J., Brau-Nogué, S., Coriat, M., et al. 2022, Nature Astronomy, 6, 503, doi: 10.1038/s41550-022-01612-3

Kohonen, T. 1990, Proceedings of the IEEE, 78, 1464, doi: 10.1109/5.58325

Le Gall, A., Bonnefoy, L., Sultana, R., et al. 2023, Icarus, 115446, doi: 10.1016/j.icarus.2023.115446

Le Gall, A., Leyrat, C., Janssen, M., et al. 2014, Icarus, 241, 221, doi: 10.1016/j.icarus.2014.06.011

Le Gall, A., West, R. D., & Bonnefoy, L. E. 2019, Geophysical Research Letters, 46, 11747, doi: 10.1029/2019GL084218

Le Gall, A., Leyrat, C., Janssen, M. A., et al. 2017, Nature Astronomy, 1, 0063, doi: 10.1038/s41550-017-0063

Leduc-Leballeur, M., Picard, G., Mialon, A., et al. 2015, IEEE Transactions on Geoscience and Remote Sensing, 53, 4022, doi: 10.1109/TGRS.2015.2388790

Lindell, D. B., & Long, D. G. 2016, IEEE Transactions on Geoscience and Remote Sensing, 54, 167, doi: 10.1109/TGRS.2015.2452215

Maeda, T., Taniguchi, Y., & Imaoka, K. 2016, IEEE Transactions on Geoscience and Remote Sensing, 54, 770, doi: 10.1109/TGRS.2015.2465170

Marc, O., Barret, M., Biancamaria, S., et al. 2024, ESS Open Archive, doi: 10.22541/essoar.170965077.73149239/v1

Markkanen, J., & Penttilä, A. 2023, Journal of Quantitative Spectroscopy and Radiative Transfer, 310, 108733, doi: 10.1016/j.jqsrt.2023.108733

Martin, E. S., Whitten, J. L., Kattenhorn, S. A., et al. 2023, Icarus, 392, 115369, doi: 10.1016/j.icarus.2022.115369

Matzler, C., Rosenkranz, P., Battaglia, A., & Wigneron, J.-P. 2006, Thermal Microwave Radiation - Applications for Remote Sensing, Vol. 52, doi: 10.1049/PBEW052E

Mergny, C., & Schmidt, F. 2024, Icarus, 413, 116008, doi: https://doi.org/10.1016/j.icarus.2024.116008

Molaro, J. L., Choukroun, M., Phillips, C. B., et al. 2019, Journal of Geophysical Research: Planets, 124, 243, doi: 10.1029/2018JE005773

Montpetit, B., Royer, A., Roy, A., Langlois, A., & Derksen, C. 2013, IEEE Transactions on Geoscience and Remote Sensing, 51, 4705, doi: 10.1109/TGRS.2013.2250509

Muinonen, K., & Penttilä, A. 2024, Journal of Quantitative Spectroscopy and Radiative Transfer, 324, 109058, doi: 10.1016/j.jqsrt.2024.109058

Ostro, S., West, R., Wye, L., et al. 2010, Icarus, 206, 498, doi: 10.1016/j.icarus.2009.07.041

Ostro, S. J., & Shoemaker, E. M. 1990, Icarus, 85, 335, doi: 10.1016/0019-1035(90)90121-O

Ostro, S. J., West, R. D., Janssen, M. A., et al. 2006, Icarus, 183, 479, doi: 10.1016/j.icarus.2006.02.019

Picard, G., Brucker, L., Fily, M., Gallée, H., & Krinner, G. 2009, Journal of Glaciology, 55, 537, doi: 10.3189/002214309788816678

Picard, G., Brucker, L., Roy, A., et al. 2013, Geoscientific Model Development, 6, 1061, doi: 10.5194/gmd-6-1061-2013

Picard, G., Domine, F., Krinner, G., Arnaud, L., & Lefebvre, E. 2012, Nature Climate Change, 2, 795, doi: 10.1038/nclimate1590

Picard, G., Löwe, H., & Mätzler, C. 2022a, The Cryosphere, 16, 3861, doi: 10.5194/tc-16-3861-2022

Picard, G., Royer, A., Arnaud, L., & Fily, M. 2014, The Cryosphere, 8, 1105, doi: 10.5194/tc-8-1105-2014

Picard, G., Sandells, M., & Löwe, H. 2018, Geoscientific Model Development, 11, 2763, doi: 10.5194/gmd-11-2763-2018

Picard, G., Löwe, H., Domine, F., et al. 2022b, AGU Advances, 3, doi: 10.1029/2021AV000630

Porter, S. B., Desch, S. J., & Cook, J. C. 2010, Icarus, 208, 492, doi: 10.1016/j.icarus.2010.01.031

Proksch, M., Mätzler, C., Wiesmann, A., et al. 2015, Geoscientific Model Development, 8, 2611, doi: 10.5194/gmd-8-2611-2015

Ries, P. A., & Janssen, M. 2015, Icarus, 257, 88, doi: 10.1016/j.icarus.2015.04.030

Rignot, E. 1995, Journal of Geophysical Research, 100, 9389, doi: 10.1029/95JE00485

Rignot, E. J., Ostro, S. J., van Zyl, J. J., & Jezek, K. C. 1993, Science, 261, 1710, doi: 10.1126/science.261.5129.1710

https://doi.org/10.5194/egusphere-2024-3972
Preprint. Discussion started: 20 March 2025

Rosenkranz, P. 2017, Remote Sens. Code Library, doi: 10.21982/M81013

Scambos, T., Frezzotti, M., Haran, T., et al. 2012, Journal of Glaciology, 58, 633, doi: 10.3189/2012JoG11J232

Soriot, C., Picard, G., Prigent, C., Frappart, F., & Domine, F. 2022, Remote Sensing of Environment, 278, 113061, doi: 10.1016/j.rse.2022.113061

Stefko, M., Leinss, S., Frey, O., & Hajnsek, I. 2022, The Cryosphere, 16, 2859, doi: 10.5194/tc-16-2859-2022

Taffin, C., Grasset, O., Le Menn, E., et al. 2012, Planetary and Space Science, 61, 124, doi: 10.1016/j.pss.2011.08.015

Tan, S., Aksoy, M., Brogioni, M., et al. 2015, IEEE Journal of Selected Topics in Applied Earth Observations and Remote Sensing, 8, 3681, doi: 10.1109/JSTARS.2015.2403286

Torquato, S., & Kim, J. 2021, Physical Review X, 11, 021002, doi: 10.1103/PhysRevX.11.021002

Traversa, G., Fugazza, D., & Frezzotti, M. 2023, The Cryosphere, 17, 427, doi: 10.5194/tc-17-427-2023

Van Den Broeke, M. 2008, Arctic, Antarctic, and Alpine Research, 40, 432, doi: 10.1657/1523-0430(07-021)[BROEKE]2.0.CO;2

Wilson, A. R. 2019, PhD thesis, University of Strathclyde, doi: 10.48730/nrjb-r655

Wye, L. C., Zebker, H. A., Ostro, S. J., et al. 2007, Icarus, 188, 367, doi: 10.1016/j.icarus.2006.12.008

Zhang, Z., Brown, S., Bolton, S., et al. 2023, Geophysical Research Letters, 50, e2022GL101565, doi: 10.1029/2022GL101565